Electronic Supplementary Materials

For https://doi.org/10.1631/jzus.A2600073

Comparative assessment of finite element formulations for dynamic analysis in low-permeability saturated porous media

Anhao PAN[1,2], Daosheng LING[1,2], Xiao MIAO[1,2], Jianjing ZHENG[2,3]

[1]Institute of Geotechnical Engineering, Zhejiang University, Hangzhou 310058, China
[2]MOE Key Laboratory of Soft Soils and Geoenvironmental Engineering, Zhejiang University, Hangzhou 310058, China
[3]Institute of Hypergravity Science and Technology, Zhejiang University, Hangzhou 310058, China

Section S1. Methodology

Section S1.1 The detailed expressions of submatrices and boundary condition

The detailed expressions of submatrices used in Eq. (3) are

$$\begin{cases} \boldsymbol{d} = \begin{Bmatrix} \boldsymbol{u} \\ \boldsymbol{p} \end{Bmatrix} \\ \boldsymbol{K}_{\mathrm{s}} = \int_{\Omega} \left[\boldsymbol{L}\boldsymbol{N}_u\right]^{\mathrm{T}} \boldsymbol{D}\boldsymbol{L}\boldsymbol{N}_u \mathrm{d}\Omega \\ \boldsymbol{K}_{\mathrm{sf}} = \int_{\Omega} \left[\boldsymbol{L}\boldsymbol{N}_u\right]^{\mathrm{T}} \left(\alpha \mathbf{m} \boldsymbol{N}_p\right) \mathrm{d}\Omega \\ \boldsymbol{K}_{\mathrm{f}} = \int_{\Omega} \left[\nabla \boldsymbol{N}_p\right]^{\mathrm{T}} k\gamma_{\mathrm{f}}^{-1} \nabla \boldsymbol{N}_p \mathrm{d}\Omega \\ \boldsymbol{H}_{\mathrm{f}} = \int_{\Omega} \boldsymbol{N}_p^{\mathrm{T}} \boldsymbol{N}_p Q_{\mathrm{b}}^{-1} \mathrm{d}\Omega \\ \boldsymbol{M}_{\mathrm{s}} = \int_{\Omega} \rho \boldsymbol{N}_u^{\mathrm{T}} \boldsymbol{N}_u \mathrm{d}\Omega \\ \boldsymbol{F}_{\mathrm{s}} = \int_{\Omega} \rho \boldsymbol{N}_u \boldsymbol{b} \mathrm{d}\Omega + \int_{\Gamma_t} \boldsymbol{N}_u \bar{\boldsymbol{t}} \mathrm{d}\Gamma \\ \boldsymbol{F}_{\mathrm{f}} = \int_{\Omega} \left[\nabla \boldsymbol{N}_p\right]^{\mathrm{T}} \rho_{\mathrm{f}} / \gamma_{\mathrm{f}} \boldsymbol{k}\boldsymbol{b} \mathrm{d}\Omega - \int_{\Gamma_q} \boldsymbol{N}_p \bar{\boldsymbol{q}} \mathrm{d}\Gamma \end{cases} \tag{S1}$$

where Ω denotes the computational domain; $\boldsymbol{K}_{\mathrm{s}}$ is the skeleton stiffness matrix, $\boldsymbol{D}$ is the material tangent stiffness matrix, $\boldsymbol{K}_{\mathrm{sf}}$ is the fluid-solid coupling matrix, $\boldsymbol{K}_{\mathrm{f}}$ is the permeability matrix of the pore fluid, $\boldsymbol{H}_{\mathrm{f}}$ is the compressibility matrix, $\boldsymbol{M}_{\mathrm{s}}$ is the mass matrix, $\boldsymbol{F}_{\mathrm{s}}$ and $\boldsymbol{F}_{\mathrm{f}}$ are the load vector of the solid and fluid phases, respectively.

The boundary conditions of the displacement field and the pore pressure field are

$$\begin{cases} \boldsymbol{t} = \boldsymbol{\sigma}'\boldsymbol{n} - \boldsymbol{n}\alpha\mathbf{m}p = \bar{\boldsymbol{t}}, & on\ \Gamma_t \\ \boldsymbol{u} = \bar{\boldsymbol{u}}, & on\ \Gamma_u \\ \boldsymbol{q} = \boldsymbol{k}\gamma_f^{-1}(-\nabla p + \rho_f \boldsymbol{b})\boldsymbol{n} = \bar{\boldsymbol{q}}, & on\ \Gamma_q \\ p = \bar{p}, & on\ \Gamma_p \end{cases} \tag{S2}$$

where $\bar{\boldsymbol{t}}$ and $\bar{\boldsymbol{u}}$ are the prescribed external traction and displacement, respectively; $\boldsymbol{n}$ is the outward normal vector to the boundary; Γ_t and Γ_u are the corresponding external traction and displacement boundaries, respectively, with $\Gamma_t \cup \Gamma_u = \Gamma$; $\bar{\boldsymbol{q}}$ and $\bar{p}$ are the prescribed normal fluid flux and pore pressure, respectively; Γ_q and Γ_p are the corresponding flux and pore pressure boundaries, respectively, with $\Gamma_q \cup \Gamma_p = \Gamma$.

Section S1.2 Time discretization

The Newmark method is employed to integrate the discretized system Eq. (3) in time. Supposing t_n and t_{n+1} are two points in the time domain and $\Delta t = t_{n+1} - t_n$ is the time step increment, according to the Newmark method the following assumptions are adopted, namely

$$\boldsymbol{d}_{t_{n+1}} = \boldsymbol{d}_{t_n} + \dot{\boldsymbol{d}}_{t_n}\Delta t + \left[\left(\frac{1}{2} - \beta\right)\ddot{\boldsymbol{d}}_{t_n} + \beta\ddot{\boldsymbol{d}}_{t_{n+1}}\right]\Delta t^2 \tag{S3}$$

$$\dot{\boldsymbol{d}}_{t_{n+1}} = \dot{\boldsymbol{d}}_{t_n} + \left[(1-\delta)\ddot{\boldsymbol{d}}_{t_n} + \delta\ddot{\boldsymbol{d}}_{t_{n+1}}\right]\Delta t \tag{S4}$$

where the subscript "$_{t_n}$" and "$_{t_{n+1}}$" represent the variables corresponding to the time t_n and t_{n+1}, respectively.

Substituting Equations (S3) and (S4) into Eq. (3), the equilibrium equation at time t_{n+1} is derived

$$\begin{bmatrix} \dfrac{1}{\beta(\Delta t)^2}\boldsymbol{M}_{\mathrm{s}} + \boldsymbol{K}_{\mathrm{s}} & -\boldsymbol{K}_{\mathrm{sf}} \\ \dfrac{\delta}{\beta\Delta t}\boldsymbol{K}_{\mathrm{sf}}{}^{\mathrm{T}} & \boldsymbol{K}_{\mathrm{f}} + \dfrac{\delta}{\beta\Delta t}\boldsymbol{H}_{\mathrm{f}} \end{bmatrix} \begin{Bmatrix} \boldsymbol{u}_{t_{n+1}} \\ \boldsymbol{p}_{t_{n+1}} \end{Bmatrix} = \begin{Bmatrix} \boldsymbol{F}_{\mathrm{s}}^{t_{n+1}} + \boldsymbol{M}_{\mathrm{s}}\left(\left(\dfrac{1}{2\beta} - 1\right)\ddot{\boldsymbol{u}}_{t_n} + \dfrac{1}{\beta\Delta t}\dot{\boldsymbol{u}}_{t_n} + \dfrac{1}{\beta(\Delta t)^2}\boldsymbol{u}_{t_n}\right) \\ \boldsymbol{F}_{\mathrm{f}}^{t_{n+1}} + \left(\dfrac{\delta}{\beta} - 1\right)\left(\boldsymbol{K}_{\mathrm{sf}}{}^{\mathrm{T}}\dot{\boldsymbol{u}}_{t_n} + \boldsymbol{H}_{\mathrm{f}}\dot{\boldsymbol{p}}_{t_n}\right) + \dfrac{\delta}{\beta\Delta t}\left(\boldsymbol{K}_{\mathrm{sf}}{}^{\mathrm{T}}\boldsymbol{u}_{t_n} + \boldsymbol{H}_{\mathrm{f}}\boldsymbol{p}_{t_n}\right) \end{Bmatrix} \tag{S5}$$

When the permeability coefficient is particularly small, the elements in $\boldsymbol{K}_{\mathrm{f}}$ is prone to zero; The elements in $\boldsymbol{H}_{\mathrm{f}}$ also approach zero when the bulk modulus of the solid and fluid phases is large. Thus, for low-permeability and incompressible porous media, $\boldsymbol{K}_\mathrm{f} + \frac{\delta}{\beta \Delta t}\boldsymbol{H}_\mathrm{f}$ is extremely small compared to $\frac{1}{\beta (\Delta t)^2}\boldsymbol{M}_\mathrm{s} + \boldsymbol{K}_\mathrm{s}$, leading to a severely ill-conditioned coefficient matrix.

Note that Eq. (S5) is a system of linear algebraic equations whose coefficient matrix is asymmetric, a more efficient symmetric coefficient matrix can be obtained by multiplying the continuity equation by the coefficient $-\frac{\beta \Delta t}{\delta}$.

Section S1.3 The submatrices of the cover function enriched element

Substituting Eq. (12) into Eqs. (1) and (2) and applying the Galerkin method for spatial discretization yields the submatrices of the discretized cover element, each component in Eq. (S1) can be rewritten as

$$\begin{cases} \boldsymbol{d} = \begin{Bmatrix} \boldsymbol{d}_u \\ \boldsymbol{d}_p \end{Bmatrix} \\ \boldsymbol{K}_\mathrm{s} = \int_\Omega \left[\boldsymbol{L}\left(\boldsymbol{N}_u \boldsymbol{P}_u \right) \right]^\mathrm{T} \boldsymbol{D}\boldsymbol{L}\left(\boldsymbol{N}_u \boldsymbol{P}_u \right) \mathrm{d}\Omega \\ \boldsymbol{K}_\mathrm{sf} = \int_\Omega \left[\boldsymbol{L}\left(\boldsymbol{N}_u \boldsymbol{P}_u \right) \right]^\mathrm{T} \left(\alpha \mathbf{m} \boldsymbol{N}_p \boldsymbol{P}_p \right) \mathrm{d}\Omega \\ \boldsymbol{K}_\mathrm{f} = \int_\Omega \left[\nabla \left(\boldsymbol{N}_p \boldsymbol{P}_p \right) \right]^\mathrm{T} k \gamma_\mathrm{f}^{-1} \nabla \left(\boldsymbol{N}_p \boldsymbol{P}_p \right) \mathrm{d}\Omega \\ \boldsymbol{H}_\mathrm{f} = \int_\Omega \left[\boldsymbol{N}_p \boldsymbol{P}_p \right]^\mathrm{T} \boldsymbol{N}_p \boldsymbol{P}_p Q_\mathrm{b}^{-1} \mathrm{d}\Omega \\ \boldsymbol{M}_\mathrm{s} = \int_\Omega \rho \left[\boldsymbol{N}_u \boldsymbol{P}_p \right]^\mathrm{T} \boldsymbol{N}_u \boldsymbol{P}_p \mathrm{d}\Omega \\ \boldsymbol{F}_\mathrm{s} = \int_\Omega \rho \boldsymbol{N}_u \boldsymbol{P}_u^\mathrm{T} \boldsymbol{b} \mathrm{d}\Omega + \int_{\Gamma_t} \boldsymbol{N}_u \boldsymbol{P}_u^\mathrm{T} \bar{\boldsymbol{t}} \mathrm{d}\Gamma,\ \boldsymbol{F}_\mathrm{f} = \int_\Omega \left[\nabla \left(\boldsymbol{N}_p \boldsymbol{P}_p \right) \right]^\mathrm{T} \rho_\mathrm{f} / \gamma_\mathrm{f} \boldsymbol{k}\boldsymbol{b} \mathrm{d}\Omega - \int_{\Gamma_q} \boldsymbol{N}_p \boldsymbol{P}_p^\mathrm{T} \bar{\boldsymbol{q}} \mathrm{d}\Gamma \end{cases} \tag{S6}$$

Section S1.4 Types of Element

Table S1. Types of Element

Element Abbreviation	Element Description	Element Geometry	Number of nodes		Number of Integration Points	Application Problem
			Solid	Pressure		
U1P1	Standard Equal Order Element	Quadrilateral	4	4	2*2	1D
		Triangle	3	3	1	2D
U1P1M	Stabilized Equal Order Element	Quadrilateral	4	4	2*2	1D
		Triangle	3	3	1	2D

U2P1	Cover Function Enriched Element	Quadrilateral	4	4	3*3	1D
		Triangle	3	3	3	2D
TH-Quad	Conventional Higher Order Element	Quadrilateral	8	4	3*3	1D

Section S2. Dynamic analysis of incompressible saturated porous media

Section S2.1 Relative pore pressure error

To provide a further illustration of the accuracy of the various elements, Fig. S1 shows the curves of the relative pore pressure error with respect to the number of elements at a height of 9 m. When the number of elements is small, the accuracy of U1P1M is superior to that of TH-Quad and U2P1. However, as the number of elements increases, the relative error of U1P1M rapidly reaches a stable value of approximately 1×10^{-4}. Ultimately, its accuracy is surpassed by U2P1. In summary, under conditions where both the skeletal and fluid materials are incompressible and permeability is low, the stabilized element U1P1M, the conventional unequal order element TH-Quad, and the cover function enriched element U2P1 all demonstrate a good ability to suppress non-physical oscillations in pore pressure.

Fig. S2 illustrates the pore pressure profiles at time $t = 0.0419$ s for permeability coefficients of $k = 1\times10^{-9}$ m/s and $k = 1\times10^{-6}$ m/s. The column is discretized into 100 elements in the vertical direction. As the permeability coefficient increases, the oscillatory behavior of pore pressure observed with U1P1 gradually diminishes. When the permeability coefficient reaches $k = 1\times10^{-6}$ m/s, oscillations are confined to a localized region at the top of the column. In contrast, all other elements maintain a stable pore pressure response throughout.

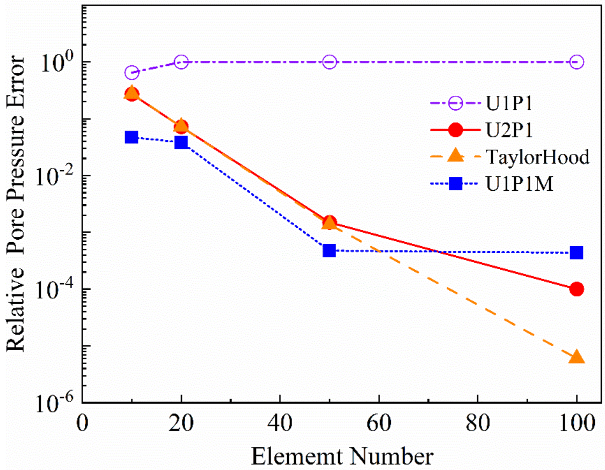

Fig. S1. Relative pore pressure error over the number of elements

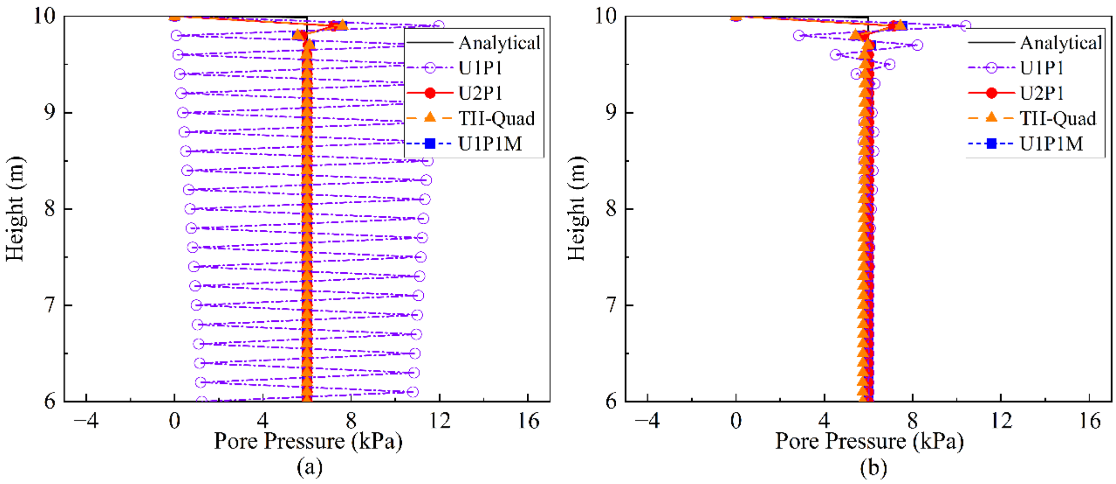

Fig. S2. Pore pressure profiles over permeability coefficient

Section S2.2 Evolution of pore pressure at nodes A and B

To provide a quantitative evaluation of the three elements, Fig. S3 and S4 illustrate the evolution of pore pressure at points A and B when the Young's modulus E is 0.3 MPa and 30 MPa, respectively. As illustrated in Fig. S3, when E = 0.3 MPa, the pore pressure peak for U1P1M occurs later than the others, with a significantly higher peak pore pressure. In addition, the pore pressure variation in U1P1M is not aligned with the loading history, and the pore pressure variation due to the skeleton vibrations after 0.04 s is also considerably larger than that observed in the other elements. As illustrated in Fig. S4, for E = 30 MPa, the pore pressure variations of U2P1 and U1P1M are mostly in agreement. However, there are some minor fluctuations in

U1P1M prior to 0.1 s, which can be attributed to the introduction of the stabilization term that disrupts the incompressibility of the material. As shown in Fig. S3 and S4, the peak pore pressure of U1P1 in response to the impulse load is higher than that of U2P1, particularly at point B. Additionally, the pore pressure variation caused by skeleton vibrations after 0.04 s at nodes A and B also differs from that observed in U2P1 and U1P1M.

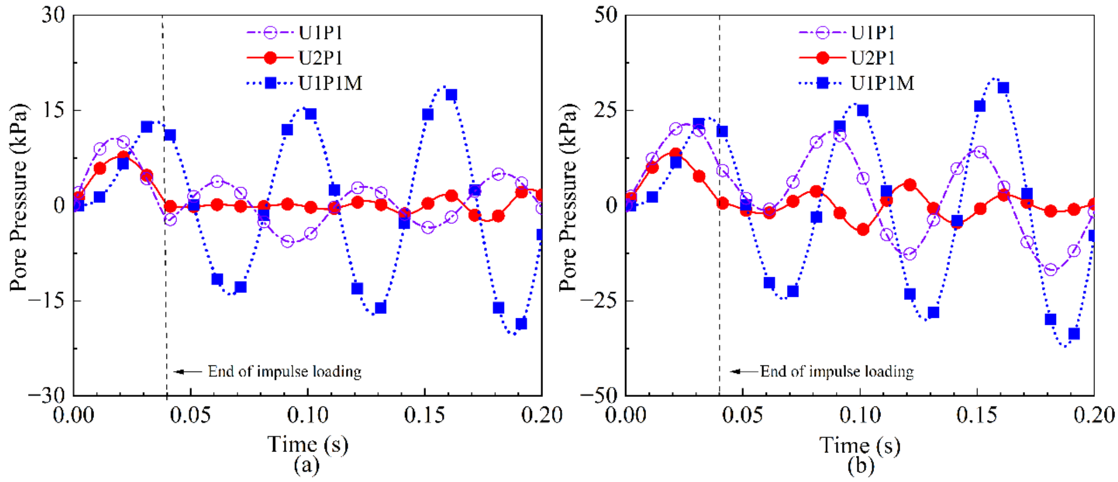

Fig. S3. Evolution of pore pressure when *E* = 0.3 MPa: (a)Node A, (b)Node B

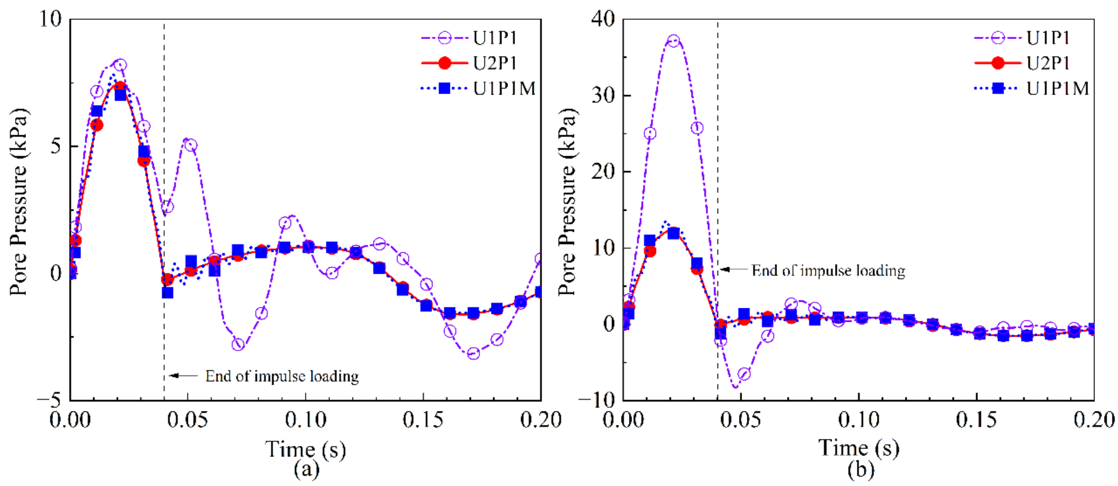

Fig. S4. Evolution of pore pressure when *E* = 30 MPa: (a)Node A, (b)Node B

In dynamic analysis of incompressible saturated porous media, U1P1 always leads to significant pore pressure oscillations at low permeability. Even a more refined mesh may prove ineffective in alleviating the non-physical oscillations for the equal order element. In the case of incompressible materials, the high accuracy of U1P1M is only possible when the stiffness of the solid skeleton is substantial. Since the artificial stabilization term violates the incompressibility of the solid and fluid phases, U1P1M is not applicable in the case of low skeleton stiffness. Even after adjusting the stabilization parameter to mitigate the effect of the stabilization term on the material properties, the desired results remain unattainable. U2P1 is capable of accurately reflecting the pore pressure response of incompressible saturated porous media in all cases and thus has a wide range of applications.

Section S3. Dynamic analysis of compressible saturated porous media

Fig. S5 illustrates the evolution of pore pressure at observation points A, B, C, and D. Compared to U1P1, the pore pressure variation obtained from U2P1 remains relatively stable. In contrast, U1P1 exhibits pronounced spurious oscillations in pore pressure. As the propagation distance increases, the magnitude of these non-physical oscillations approaches or even exceeds that of the actual wave-induced pore pressure. Moreover, the wave velocity gradually decreases relative to that of U2P1. While U1P1M yields a stable pore pressure evolution, the significant underestimation of both the pore pressure magnitude and the wave velocity leads to a substantial deviation from the actual dynamic response of saturated porous media.

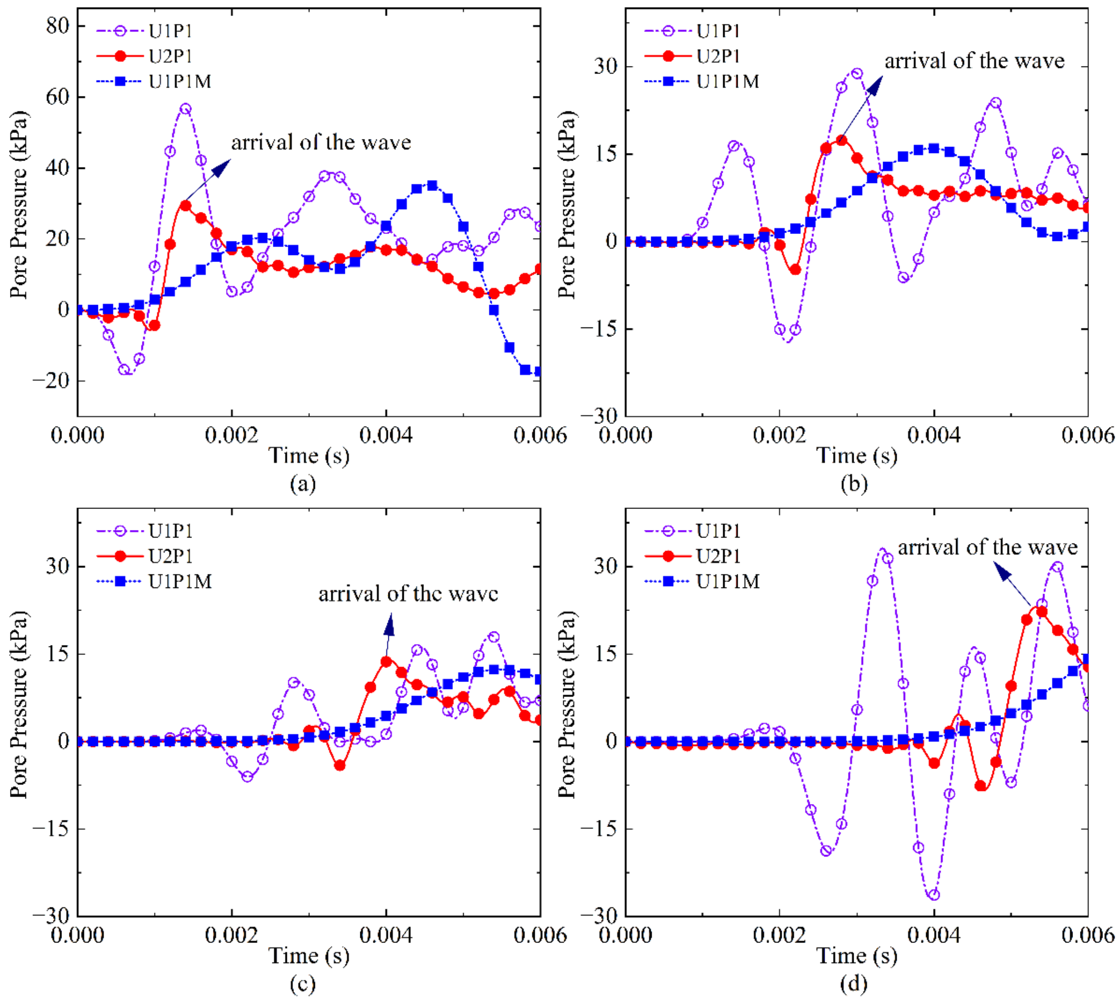

Fig. S5. Evolution of pore pressure: (a) Node A, (b) Node B, (c) Node C, (d) Node D

In compressible saturated porous media, U1P1 exhibits unphysical oscillations under most conditions, but the oscillations are mitigated when the solid skeleton stiffness is considerable. By introducing an artificial stabilization term, U1P1M circumvents spurious pore pressure oscillations. However, this approach fundamentally alters the mechanical properties of the material, leading to pronounced errors in the waveforms, amplitudes, and velocities of compressional waves. It remains challenging to achieve accurate and stable results for U1P1M even after modifying the stabilization parameters. U2P1 enriched with high-order covering functions has shown robust performance in simulations of pore pressure evolution in compressible porous media. It can consistently reproduce the propagation of compressional waves under the influence of both macroscopic and microscopic compressibility, without compromising accuracy or stability.